Hindawi
Journal of Function Spaces
Volume 2022, Article ID 2970876, 11 pages
https://doi.org/10.1155/2022/2970876

Research Article

Linear Stability Analysis of the Cahn–Hilliard Equation in Spinodal Region

Seokjun Ham,[1] Darae Jeong,[2] Hyundong Kim,[3] Chaeyoung Lee,[1] Soobin Kwak,[1] Youngjin Hwang,[1] and Junseok Kim[1]

[1]*Department of Mathematics, Korea University, Seoul 02841, Republic of Korea*
[2]*Department of Mathematics, Kangwon National University, Gangwon-do 24341, Republic of Korea*
[3]*Institute for the Advanced Study of Human Biology (WPI-ASHBi), Kyoto University Institute for Advanced Study, Kyoto University, Kyoto 6068315, Japan*

Correspondence should be addressed to Junseok Kim; cfdkim@korea.ac.kr

Received 12 April 2022; Accepted 6 June 2022; Published 24 June 2022

Academic Editor: Mitsuru Sugimoto

We study a linear stability analysis for the Cahn–Hilliard (CH) equation at critical and off-critical compositions. The CH equation is solved by the linearly stabilized splitting scheme and the Fourier-spectral method. We define the analytic and numerical growth rates and compare these growth rates with respect to the different average levels. In this study, the linear stability analysis is conducted by classifying three average levels such as zero average, spinodal average, and near critical point levels of free energy function, in the one-dimensional (1D) space. The numerical results provide insight for the dynamics of CH equation at critical and off-critical compositions.

1. Introduction

The Cahn–Hilliard (CH) equation describes the temporal evolution of the conserved phase-field by the following partial differential equation [1, 2]:

$$\frac{\partial \phi(x,t)}{\partial t} = \Delta\left[F'(\phi(x,t)) - \varepsilon^2 \Delta\phi(x,t)\right], x \in \Omega, t > 0, \quad (1)$$

where $\phi(x,t)$ is a phase-field at position x and time t, $F(\phi) = 0.25(\phi^2 - 1)^2$ is the free energy per unit volume and can be substituted for other free energy functions in numerical experiments, and constant ε determines the thickness of the interface. The CH equation (1) was originally introduced as the mathematical model which describes the spinodal decomposition in a binary mixture. This equation has been applied in diverse fields such as dealloying [3, 4], two-phase fluid flow [5–7], topology optimization [8–10], population dynamics [11], tumor growth [12–14], thin films [15–17], block copolymer [18, 19], and image processing [20, 21]. The CH equation is mass-constrained gradient flow in the dual space H^{-1} of zero average space of the Ginzburg–Landau free energy,

$$\mathcal{E}(\phi) := \int_\Omega \left(F(\phi) + \frac{\varepsilon^2}{2}|\nabla\phi|^2\right) dx. \quad (2)$$

To confirm the total mass conservation and the energy dissipation, we differentiate the total mass of ϕ and equation (2) with respect to time t and obtain the following results, respectively.

$$\frac{d}{dt}\int_\Omega \phi dx = \int_\Omega \phi_t dx = \int_\Omega \Delta\left[F'(\phi) - \varepsilon^2\Delta\phi\right] dx = 0, \quad (3)$$

$$\begin{aligned}\frac{d}{dt}\mathcal{E}(\phi) &= \int_\Omega \left(F'(\phi)\phi_t + \varepsilon^2 \nabla\phi\cdot\nabla\phi_t\right) dx \\ &= \int_\Omega \left(F'(\phi) - \varepsilon^2\Delta\phi\right)\phi_t dx \\ &= -\int_\Omega \left|\nabla\left(F'(\phi) - \varepsilon^2\Delta\phi\right)\right|^2 dx \le 0.\end{aligned} \quad (4)$$

The results of equations (3) and (4), respectively, show that the conservation of total mass holds, and the total energy does not increase with respect to time. Figure 1 represents a double-well potential $F(\phi)$, its corresponding first and second derivatives. Here, the spinodal region is defined by the gray-colored region where the second derivative is negative, i.e., $F''(\phi) < 0$. In this region, ϕ is unstable and then phase separation occurs. With these various applications of the CH equation, many researchers have proposed new efficient numerical methods [22–24]. Usually, in the stage of verifying the numerical method, the linear stability analysis is used. In [25], the linear stability was used for local equilibrium of Boltzmann equation. In [26], the stability analysis of the advective CH equation was employed to define the perturbation to investigate the instability of wave packets. In this paper, we shall present a clear standard for this test by defining linear and nonlinear regimes.

The main purpose of this paper is to numerically investigate the dynamics of phase separation in binary mixtures with different average concentrations using the CH equation in the one-dimensional (1D) space. In addition, we propose criteria for linear regimes with small differences between numerical solutions and linear solutions.

This paper is organized as follows. The Fourier-spectral method is introduced in Section 2 for numerical solution. Section 3 provides numerical results and simulations with linear stability analysis. Conclusions are discussed in Section 4.

2. Numerical Solution

Now, we use the Fourier-spectral method [27] to find the numerical solution for the CH equation (1) in the 1D space $\Omega = (0, L)$,

$$\frac{\partial \phi(x,t)}{\partial t} = \Delta\left[F'(\phi(x,t)) - \varepsilon^2 \Delta \phi(x,t)\right], x \in (0,L), t > 0. \quad (5)$$

Let $h = L/N_x$ be the grid size in the x-axis directions, where N_x is positive even integer. At the edge points $x_m = (m-1)h$ where $m = 1, 2, \cdots, N_x$, we simply denote the numerical representation $\phi(x_m, t_n)$ into ϕ_m^n. Here, $t_n = n\Delta t$ and Δt is the temporal step size. Also, we set $\mu_p = 2\pi p/L$ for the Fourier-spectral method. Let us consider the discrete Fourier transform $\widehat{\phi}_p^n = \sum_{m=1}^{N_x} \phi_m^n e^{-i(\mu_p x_m)}$ and the inverse discrete Fourier transform

$$\phi_m^n = \frac{1}{N_x} \sum_{p=-N_x/2}^{N_x/2-1} \widehat{\phi}_p^n e^{i(\mu_p x_m)}. \quad (6)$$

For simplicity of notation, we define $f(\phi) = F'(\phi) = \phi^3 - \phi$. By applying the linearly stabilized splitting scheme [28] into the CH equation (5), we obtain the following discrete CH equation:

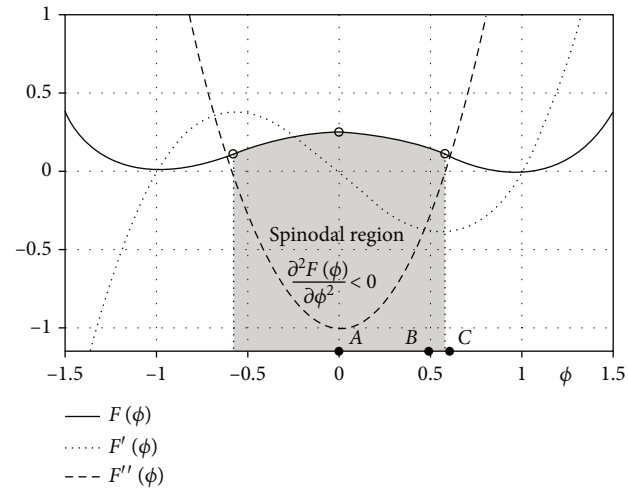

Figure 1: Schematic illustration of double-well potential $F(\phi)$, $F'(\phi)$, and $F''(\phi)$.

$$\begin{aligned}\frac{\phi_m^{n+1} - \phi_m^n}{\Delta t} &= \Delta\left[f(\phi_m^n) - 2\phi_m^n + 2\phi_m^{n+1} - \varepsilon^2 \Delta \phi_m^{n+1}\right] \\ &= \Delta\left[(\phi_m^n)^3 - 3\phi_m^n + 2\phi_m^{n+1} - \varepsilon^2 \Delta \phi_m^{n+1}\right].\end{aligned} \quad (7)$$

Letting $g(\phi) = \phi^3 - 3\phi$, equation (7) comes into

$$\frac{\phi_m^{n+1} - \phi_m^n}{\Delta t} = \Delta\left[g(\phi_m^n) + 2\phi_m^{n+1} - \varepsilon^2 \Delta \phi_m^{n+1}\right]. \quad (8)$$

Then, we can transform equation (8) into the discrete Fourier space as follows:

$$\frac{\widehat{\phi}_p^{n+1} - \widehat{\phi}_p^n}{\Delta t} = \mu_p^2\left[2\widehat{\phi}_p^{n+1} + \varepsilon^2 \mu_p^2 \widehat{\phi}_p^{n+1} + \widehat{g}_p^n\right]. \quad (9)$$

By rearranging the above one, we obtain

$$\widehat{\phi}_p^{n+1} = \frac{\widehat{\phi}_p^n - \mu_p^2 \Delta t \widehat{g}_p^n}{1 + \Delta t\left(2\mu_p^2 + \varepsilon^2 \mu_p^4\right)}. \quad (10)$$

As a consequence, we can compute the updated numerical solution ϕ_m^{n+1} by applying the inverse discrete Fourier transform (6).

3. Numerical Experiments

In this section, we define growth rate of the CH equation and compare analytic growth rate with numerical growth rate. We also define an error between the analytic solution and the numerical solution. Through several numerical experiments about the growth rate and the error, we investigate the numerical behaviour at different spinodal points. Then, we propose linear and nonlinear regimes.

3.1. Analytic and Numerical Growth Rates. In this section, we shall find the analytic and numerical growth rates. We

consider the following three different free energy functions [29], F_1, F_2, and F_3 at $\phi = \phi_{ave}$.

$$F_1(\phi) = 0.25\left(\phi^2 - 1\right)^2, \tag{11}$$

$$F_2(\phi) = \phi^6 - \phi^4 - \phi^2 + 1, \tag{12}$$

$$F_3(\phi) = 0.5\left((1+\phi)\ln\left(\frac{1+\phi}{2}\right) + (1-\phi)\ln\left(\frac{1-\phi}{2}\right)\right) + 1.695\left(1-\phi^2\right). \tag{13}$$

We linearize each of F'_1, F'_2, and F'_3 by applying the Taylor expansion for different free energy functions; then, we obtain the following linearized terms. The linearized functions are explained in detail in Appendix.

$$F'_1(\phi) \approx \phi_{ave}^3 - \phi_{ave} + \left(3\phi_{ave}^2 - 1\right)(\phi - \phi_{ave}), \tag{14}$$

$$F'_2(\phi) \approx 6\phi_{ave}^5 - 4\phi_{ave}^3 - 2\phi_{ave} + 2\left(15\phi_{ave}^4 - 6\phi_{ave}^2 - 1\right)(\phi - \phi_{ave}), \tag{15}$$

$$F'_3(\phi) \approx 0.5\ln\left(\frac{1+\phi_{ave}}{1-\phi_{ave}}\right) - 3.39\phi_{ave} + \left(\frac{1}{2(1+\phi_{ave})} + \frac{1}{2(1-\phi_{ave})} - 3.39\right)(\phi - \phi_{ave}). \tag{16}$$

Therefore, for the free energy functions F_1, F_2, and F_3, the corresponding linear Cahn–Hilliard (LCH) equations are as follows:

$$\frac{\partial\phi(x,t)}{\partial t} = \left(3\phi_{ave}^2 - 1\right)\Delta\phi(x,t) - \varepsilon^2\Delta^2\phi(x,t), \tag{17}$$

$$\frac{\partial\phi(x,t)}{\partial t} = 2\left(15\phi_{ave}^4 - 6\phi_{ave}^2 - 1\right)\Delta\phi(x,t) - \varepsilon^2\Delta^2\phi(x,t), \tag{18}$$

$$\frac{\partial\phi(x,t)}{\partial t} = \left(\frac{1}{2(1+\phi_{ave})} + \frac{1}{2(1-\phi_{ave})} - 3.39\right) \cdot \Delta\phi(x,t) - \varepsilon^2\Delta^2\phi(x,t). \tag{19}$$

To derive the ordinary differential equation for amplitude function $\alpha(t)$, we take $\phi(x,t) = \phi_{ave} + \alpha(t)\cos(K\pi x)$. For the positive even integer K, it can satisfy the periodic boundary condition. Substituting above $\phi(x,t)$ into LCH equations (17), (18), and (19), we have

$$\alpha'(t)\cos(K\pi x) = \left(1 - 3\phi_{ave}^2\right)\alpha(t)(K\pi)^2\cos(K\pi x) - \varepsilon^2\alpha(t)(K\pi)^4\cos(K\pi x), \tag{20}$$

$$\alpha'(t)\cos(K\pi x) = 2\left(1 + 6\phi_{ave}^2 - 15\phi_{ave}^4\right)\alpha(t)(K\pi)^2 \cdot \cos(K\pi x) - \varepsilon^2\alpha(t)(K\pi)^4\cos(K\pi x), \tag{21}$$

$$\alpha'(t)\cos(K\pi x) = \left(3.39 - \frac{1}{2(1+\phi_{ave})} - \frac{1}{2(1-\phi_{ave})}\right) \cdot \alpha(t)(K\pi)^2\cos(K\pi x) - \varepsilon^2\alpha(t)(K\pi)^4 \cdot \cos(K\pi x). \tag{22}$$

Dividing $\cos(K\pi x)$ on the both sides of equations (20), (21), and (22), we obtain

$$\alpha'(t) = (K\pi)^2\left[1 - 3\phi_{ave}^2 - \varepsilon^2(K\pi)^2\right]\alpha(t), \tag{23}$$

$$\alpha'(t) = (K\pi)^2\left[2 + 12\phi_{ave}^2 - 30\phi_{ave}^4 - \varepsilon^2(K\pi)^2\right]\alpha(t), \tag{24}$$

$$\alpha'(t) = (K\pi)^2\left[3.39 - \frac{1}{2(1+\phi_{ave})} - \frac{1}{2(1-\phi_{ave})} - \varepsilon^2(K\pi)^2\right]\alpha(t). \tag{25}$$

The analytic solutions of ordinary differential equations (23), (24), and (25) are as follows:

$$\alpha(t) = \alpha(0)e^{\lambda_1 t}, \lambda_1 = (K\pi)^2\left[1 - 3\phi_{ave}^2 - \varepsilon^2(K\pi)^2\right], \tag{26}$$

$$\alpha(t) = \alpha(0)e^{\lambda_2 t}, \lambda_2 = (K\pi)^2\left[2 + 12\phi_{ave}^2 - 30\phi_{ave}^4 - \varepsilon^2(K\pi)^2\right], \tag{27}$$

$$\alpha(t) = \alpha(0)e^{\lambda_3 t}, \lambda_3 = (K\pi)^2\left[3.39 - \frac{1}{2(1+\phi_{ave})} - \frac{1}{2(1-\phi_{ave})} - \varepsilon^2(K\pi)^2\right]. \tag{28}$$

In this paper, we use F_1 unless the free energy function is mentioned; then, we write $F_1 = F$, $\lambda_1 = \lambda$. In the numerical approach, numerical growth rate is defined by

$$\tilde{\lambda} = \frac{1}{T}\log\left(\frac{\left\|\phi^{N_t} - \phi_{ave}\right\|_\infty}{\alpha(0)}\right). \tag{29}$$

Here, $\|\cdot\|_\infty$ denotes the maximum norm.

3.2. Convergence Test. In this section, we verify convergence of the numerical growth rate. For numerical test, we use $\phi(x,0) = \phi_{ave} + 0.001\cos(10\pi x)$, $\phi_{ave} = 0$, and $\varepsilon = 0.02$ in $\Omega = (0,1)$.

Table 1 shows the numerical growth rate $\tilde{\lambda}$ at time $T = 0.004$ for various $\Delta t = T/N_t$ and $h = 1/N_x$. Here, the analytic growth rate is $\lambda = 597.3241$. In Table 1, we can see that the numerical growth rate converges to the analytic one as Δt and h decrease.

3.3. Linear Stability Analysis. From now on, we implement the linear stability analysis with the constant solution $\phi = \phi_{ave}$. In the every numerical experiment, we use the constant $\varepsilon = \varepsilon_m = mh/[2\sqrt{2}\tanh^{-1}(0.9)]$ to adjust the interfacial thickness. As long as do not more mentioned, the numerical parameters use such as $N_x = 128$, $h = 1/N_x$, Δt =2e-7, $\alpha(0) = 0.001$, $\varepsilon = \varepsilon_{11}$, and T is total time. In addition, we use three

Table 1: Numerical growth rate for various Δt and h at $T = 0.004$ ($\lambda = 597.3241$).

$N_t \setminus N_x$	2^3	2^4	2^5	2^6	2^7
2^{11}	304.2649	594.2164	594.2139	594.2139	594.2139
2^{12}	304.5360	595.7570	595.7545	595.7545	595.7545
2^{13}	304.6718	596.5303	596.5278	596.5278	596.5278
2^{14}	304.7397	596.9177	596.9152	596.9152	596.9152
2^{15}	304.7737	597.1116	597.1091	597.1091	597.1091
2^{16}	304.7907	597.2086	597.2061	597.2061	597.2061
2^{17}	304.7992	597.2571	597.2546	597.2546	597.2546

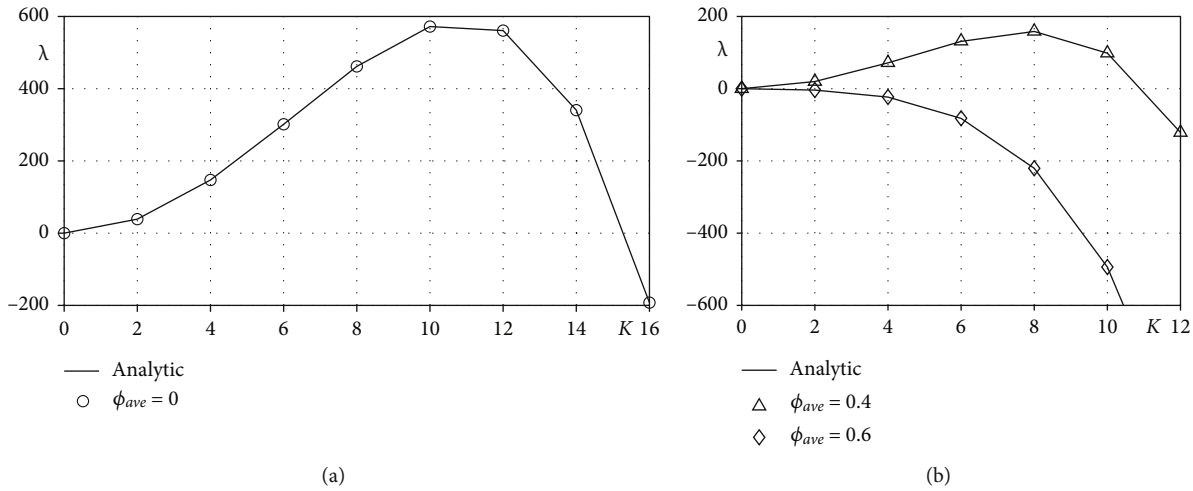

Figure 2: Analytic and numerical growth rates of the CH equation with different mode numbers at $T = 0.004$ when (a) $\phi_{ave} = 0$ and (b) $\phi_{ave} = 0.4$ and $\phi_{ave} = 0.6$.

different value $\phi_{ave} = 0, 0.4$, and 0.6 which are in spinodal region and near critical points of free energy. Note that these values are indicated points A, B, and C in Figure 1. For a positive even integer $K \leq 16$, the initial condition is selected as $\phi(x, 0) = \phi_{ave} + 0.001 \cos(K\pi x)$ in $\Omega = (0, 1)$. First, we investigate analytic and numerical growth rates for different mode numbers K.

Before the next tests, we define linear solution as follows:

$$u(x, t) = \phi_{ave} + \alpha(t) \cos(K\pi x), \tag{30}$$

where $\alpha(t) = \alpha(0)e^{\lambda t}$ and λ is analytic growth rate, see equation (26). Figure 2 shows the change of the analytic and numerical growth rates with respect to each mode numbers K for $\phi_{ave} = 0$, 0.4, and 0.6 in short-time evolution. As we can see, numerical growth rate $\tilde{\lambda}$ estimates analytic growth rate λ well in short time ($T = 0.004$). The growth rates in spinodal region ($\phi_{ave} = 0$, $\phi_{ave} = 0.4$) have positive values for some mode K. On the other hand ($\phi_{ave} = 0.6$), the growth rates are always negative regardless of mode number K and also growth rates are monotonically decreased as mode number K increases. Figures 3(a)–3(c) show the analytic growth rates according to mode numbers K for $\phi_{ave} = 0$, 0.4, and 0.6, respectively, where the analytic growth rates λ_1, λ_2, and λ_3 are (26), (27), and (28). However, in the long time evolution, it is difficult to expect the numerical growth rate that fits well with the analytic one. In order to find this reason, we first observe dynamics of the numerical solution $\phi(x, t)$ and linear solution $u(x, t)$. In Figure 4, we can check the behaviour of the numerical and linear solution in short and long time evolution for $K = 2, 4$, and 6, when $\phi_{ave} = 0$ and $\phi_{ave} = 0.4$. Unlike the short-time cases, the long-time numerical solutions in all cases show a lot of difference from the linear solutions. This result means that over time, the CH solution has nonlinearity.

Let us consider Ginzburg–Landau free energy (2) by decomposing it as

$$\mathscr{E}(\phi) = \mathscr{E}_1(\phi) + \mathscr{E}_2(\phi), \tag{31}$$

where

$$\mathscr{E}_1(\phi) = \int_\Omega F(\phi) d\mathrm{x} \text{ and } \mathscr{E}_2(\phi) = \int_\Omega \frac{\varepsilon^2}{2} |\nabla\phi|^2 d\mathrm{x}. \tag{32}$$

We compare short- and long-time numerical solution $\phi(x, t)$ when $\phi_{ave} = 0$ and $\phi_{ave} = 0.4$. In this test, we use mode $K = 2$ and $\alpha(0) = 0.1$. As shown in Figure 5(a), we can see

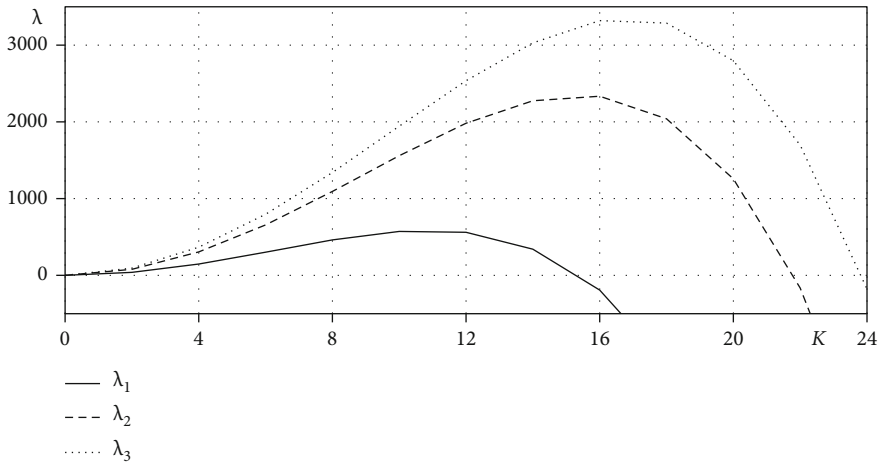

(a) $\phi_{ave} = 0$

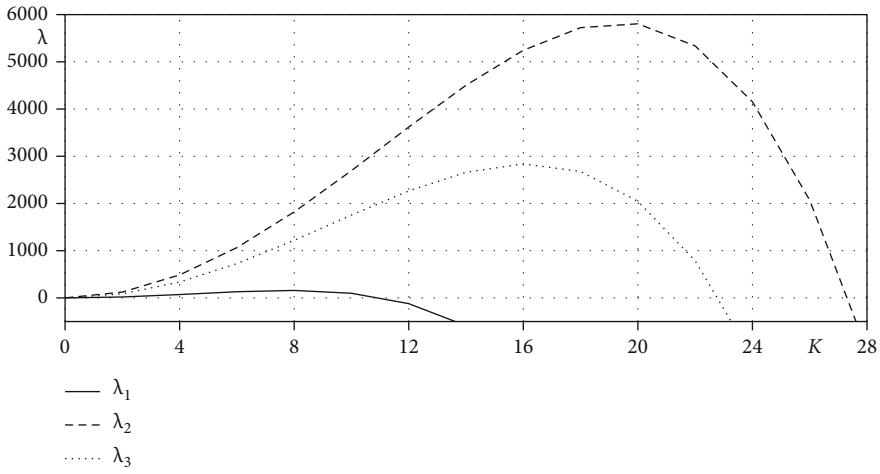

(b) $\phi_{ave} = 0.4$

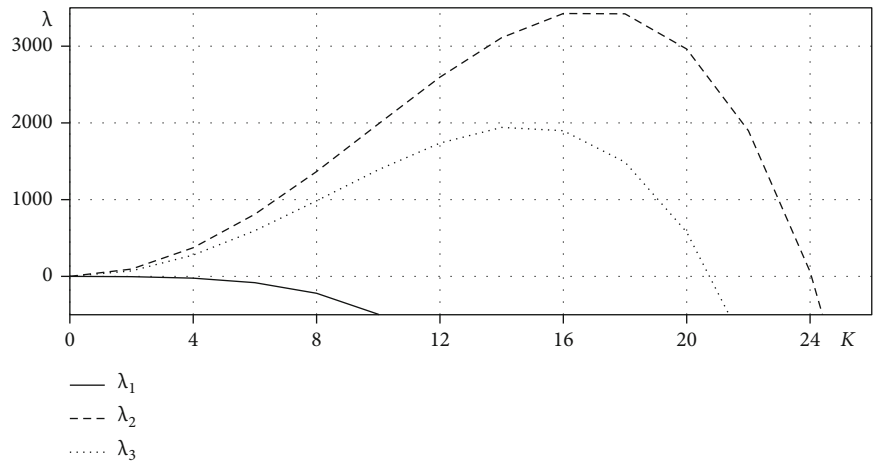

(c) $\phi_{ave} = 0.6$

FIGURE 3: Analytic growth rates of the CH equations for different free energy functions F_1, F_2, and F_3 at (a) $\phi_{ave} = 0$, (b) $\phi_{ave} = 0.4$, and (c) $\phi_{ave} = 0.6$.

the nonlinearity in the long-time solution after a certain period of time, regardless of ϕ_{ave}. Figures 5(b)–5(d) show results of double well potential $F(\phi)$, $\varepsilon/2|\nabla\phi|^2$, and $F(\phi) + \varepsilon/2|\nabla\phi|^2$, respectively. Here, the solid and dashed lines mean the short- and long-time results of each function, respectively. Also, the area of the gray-colored region in

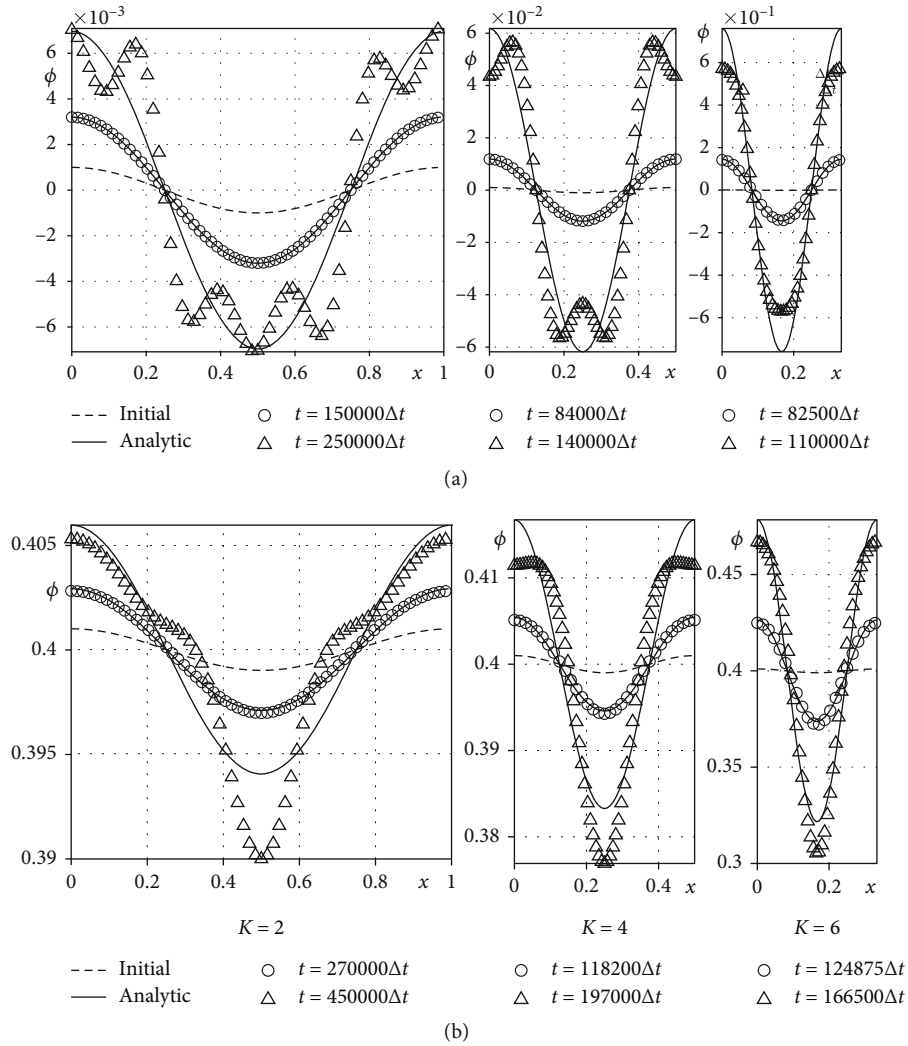

FIGURE 4: Numerical solution and theoretical solution at spinodal position (a) $\phi_{ave} = 0$ and (b) $\phi_{ave} = 0.4$ with different mode.

Figures 5(b)–5(d) represent the energy $\mathscr{E}_1(\phi)$, $\mathscr{E}_2(\phi)$, and the Ginzburg–Landau free energy $\mathscr{E}(\phi)$, respectively.

As shown in Figure 1, as ϕ moves away from $\phi = 0$, $F(\phi)$ becomes smaller than $F(0)$ when $-1 \le \phi \le 1$. For this result, in Figure 5(b), dashed line is located below solid line overall of x. It means that $F(\phi)$ becomes smaller over time in the spinodal region. Also, according to fluctuation of ϕ, we can see the property of $\varepsilon^2/2|\nabla\phi|^2$ in Figure 5(c). However, it can also be confirmed that the value has a slight effect on $F(\phi) + \varepsilon/2|\nabla\phi|^2$ as shown in Figure 5(d). In conclusion, we know that the CH solution grows with time in the spinodal region, and it has nonlinearity in the existing solution in order to reduce the total free energy.

Figures 6(a)–6(c) show temporal evolution of $\mathscr{E}_1(\phi)$, $\mathscr{E}_2(\phi)$, and $\mathscr{E}(\phi)$ with different ε. All results of $\mathscr{E}_1(\phi)$ and $\mathscr{E}(\phi)$ decrease with respect to time t. However, it can be seen that the larger the epsilon, that is, the thicker the interface of numerical solution, the slower the result is expressed.

From now on, we verify that the CH solution has nonlinearity over time. Therefore, when performing a linear stability test, it is accurate to examine short time evolution. Also, based on this fact, we propose the criteria for defining the following linear and nonlinear regimes. To find linear regime where numerical solution estimates linear solution well, we define error $e(n\Delta t)$ between numerical and linear solution as follows:

$$e(n\Delta t) = \left(\frac{1}{N_x} \sum_{m=1}^{N_x} |u(x_m, n\Delta t) - \phi_m^n|^2 \right)^{1/2}. \quad (33)$$

We can distinguish linear regime and nonlinear regime based on the user-criteria tol as follows: if $e(n\Delta t) < tol$; then, linear regime; otherwise, non-linear regime. We propose a criterion tol using the initial condition $u(x, 0)$ as follows:

$$tol = \left(\frac{1}{4N_x} \sum_{m=1}^{N_x} |u(x_m, 0)|^2 \right)^{1/2}. \quad (34)$$

Figure 7 shows proposed criterion and temporal evolution of error $e(t = n\Delta t)$ for the time t with dynamic of linear and numerical solutions.

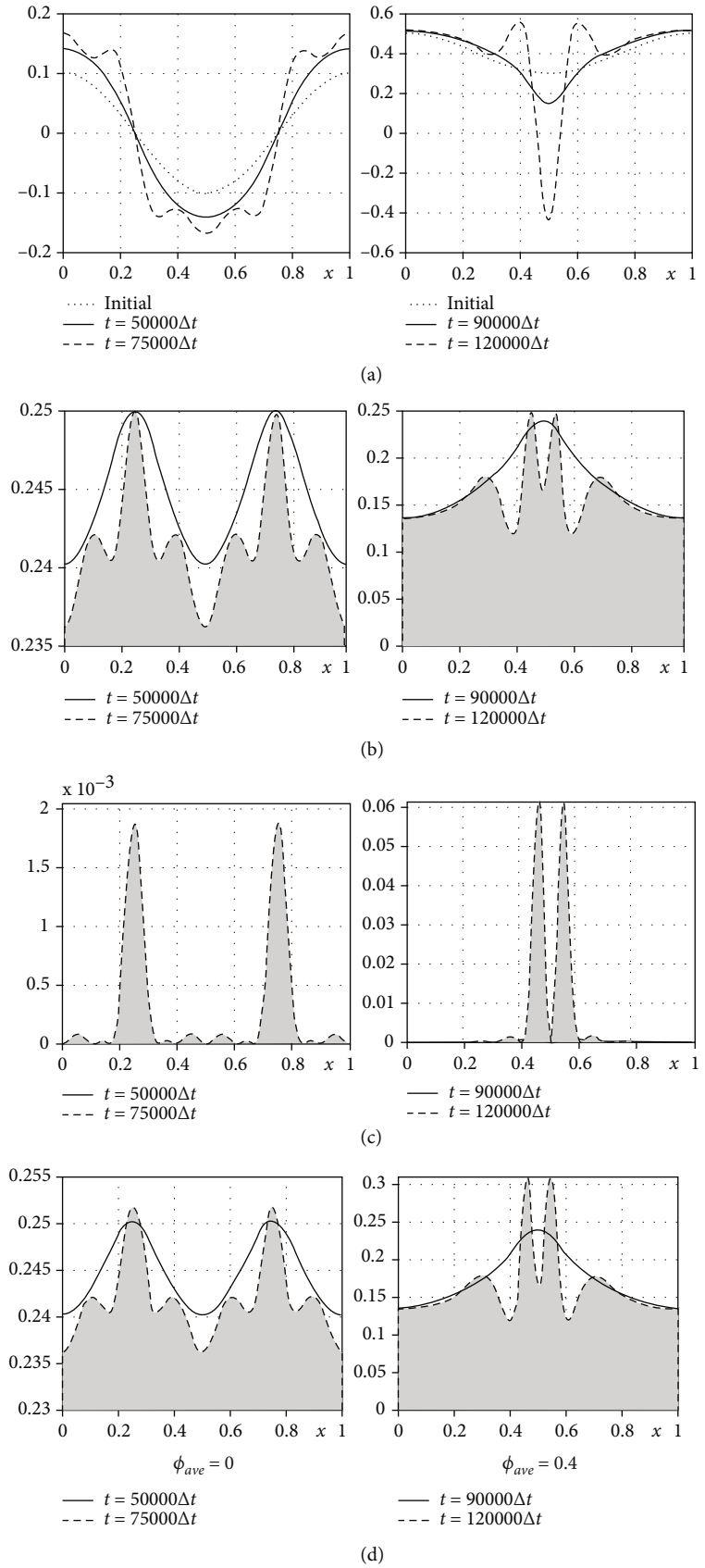

Figure 5: Long- and short-time evolutions: (a) dynamics of the CH equation, (b)–(d) terms of Ginzburg–Landau free energy $\mathscr{E}(\phi)$: $F(\phi)$, $\varepsilon^2/2|\nabla\phi|^2$, and $F(\phi) + \varepsilon^2/2|\nabla\phi|^2$, respectively.

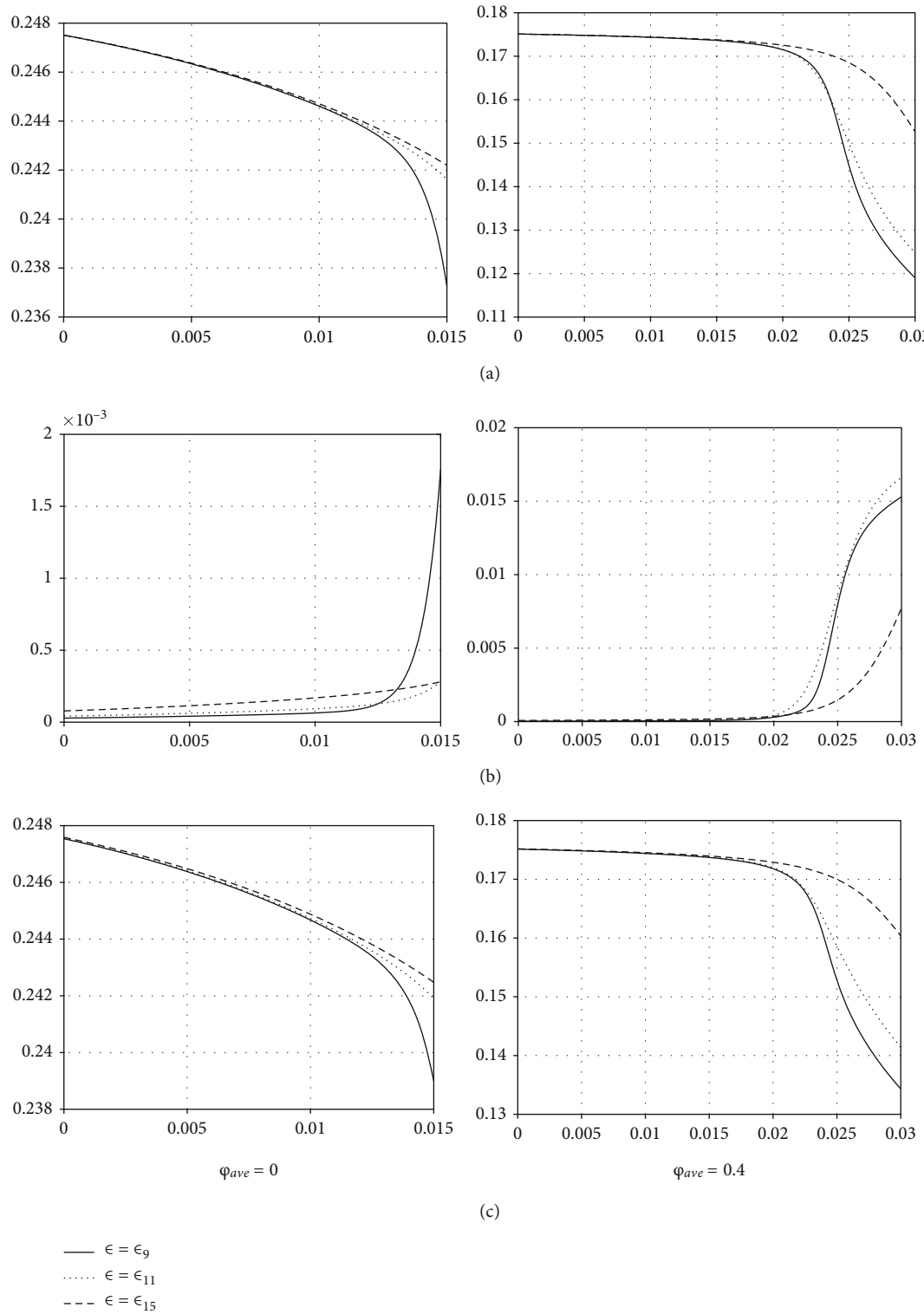

FIGURE 6: Temporal evolution of (a) $\mathscr{E}_1(\phi)$, (b) $\mathscr{E}_2(\phi)$, and (c) $\mathscr{E}(\phi)$ for each ε: ε_9, ε_{11}, and ε_{15}.

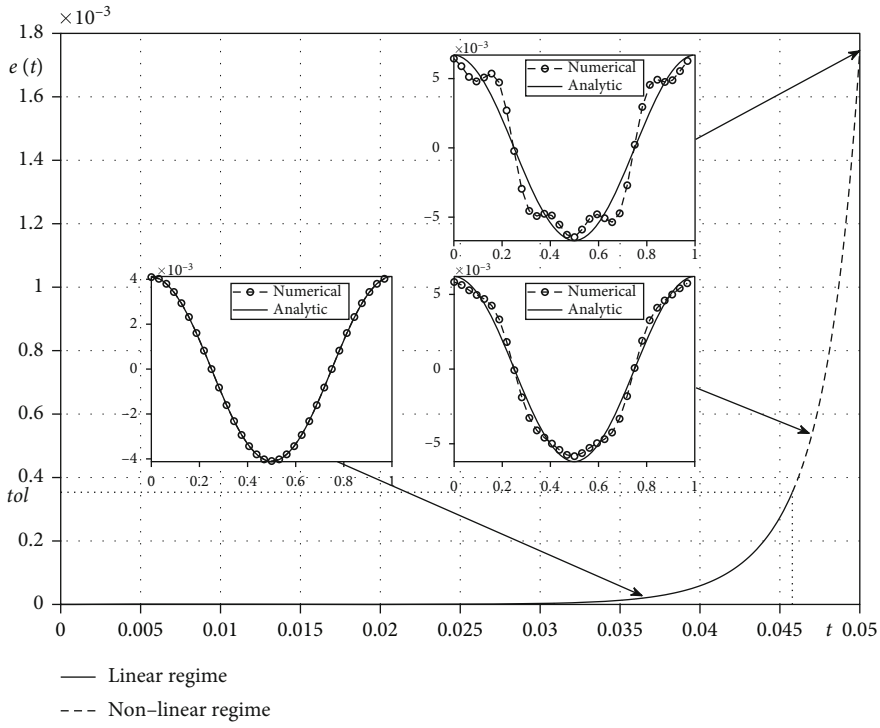

Figure 7: Temporal evolution of error $e(t = n\Delta t)$ for mode $K = 2$.

4. Conclusions

We studied a linear stability analysis for the CH equation in spinodal region as different average levels. To solve the CH equation, we used linearly stabilized splitting scheme and Fourier-spectral method. Through the numerical simulations, we observed various dynamics of the CH equation and confirmed the numerical solution compared linear solution over time. We defined growth rate and also compared numerical growth rate and analytic growth rate. Using difference between numerical and linear solution, we defined error. By means of defined error, we distinguish linear regime where numerical solution and linear solution match because of the small error and nonlinear regime where do not.

Appendix

A. Appendix: Linearlization

By the Taylor theorem, for real valued-function $f(x)$, if $f(x)$ has derivatives of all orders at a, then for each positive integer n,

$$f(x) = f(a) + f'(a)(x-a) + \frac{f''(a)}{2!}(x-a)^2 + \cdots + \frac{f^{(n)}(a)}{n!}(x-a)^n + R_n(x), \tag{A.1}$$

where $R_n(x) = \int_a^x (x-t)^n/n! f^{(n+1)}(t)dt$.

Now, we approximate the linearized functions of various free energies at ϕ_{ave}.

$$\begin{aligned} f_1(\phi) = F_1'(\phi) = \phi^3 - \phi \Rightarrow F_1'(\phi) &= \phi_{ave}^3 - \phi_{ave} + \left(3\phi_{ave}^2 - 1\right) \\ &\cdot (\phi - \phi_{ave}) + \int_{\phi_{ave}}^{x} (x-t) f_1^{(2)}(t)dt \therefore F_1'(\phi) \\ &\approx \phi_{ave}^3 - \phi_{ave} + \left(3\phi_{ave}^2 - 1\right)(\phi - \phi_{ave}), \end{aligned} \tag{A.2}$$

$$\begin{aligned} f_2(\phi) = F_2'(\phi) = 6\phi^5 - 4\phi^3 - 2\phi \Rightarrow F_2'(\phi) &= 6\phi_{ave}^5 - 4\phi_{ave}^3 \\ &- 2\phi_{ave} + 2\left(15\phi_{ave}^4 - 6\phi_{ave}^2 - 1\right)(\phi - \phi_{ave}) \\ &+ \int_{\phi_{ave}}^{x} (x-t) f_2^{(2)}(t)dt \therefore F_2'(\phi) \approx 6\phi_{ave}^5 - 4\phi_{ave}^3 \\ &- 2\phi_{ave} + 2\left(15\phi_{ave}^4 - 6\phi_{ave}^2 - 1\right)(\phi - \phi_{ave}), \end{aligned} \tag{A.3}$$

$$\begin{aligned} f_3(\phi) = F_3'(\phi) = 0.5 \ln\left(\frac{1+\phi}{1-\phi}\right) - 3.39\phi \Rightarrow F_3'(\phi) &= 0.5 \ln\left(\frac{1+\phi_{ave}}{1-\phi_{ave}}\right) - 3.39\phi_{ave} \\ &+ \left(\frac{1}{2(1+\phi_{ave})} + \frac{1}{2(1-\phi_{ave})} - 3.39\right)(\phi - \phi_{ave}) \\ &+ \int_{\phi_{ave}}^{x} (x-t) f_3^{(2)}(t)dt \therefore F_3'(\phi) \approx 0.5 \ln\left(\frac{1+\phi_{ave}}{1-\phi_{ave}}\right) \\ &- 3.39\phi_{ave} + \left(\frac{1}{2(1+\phi_{ave})} + \frac{1}{2(1-\phi_{ave})} - 3.39\right) \\ &\cdot (\phi - \phi_{ave}). \end{aligned} \tag{A.4}$$

Data Availability

No data were used to support this study.

Conflicts of Interest

The authors declare that they have no conflicts of interest.

Acknowledgments

The first author (S. Ham) was supported by the Brain Korea 21 FOUR through the National Research Foundation of Korea funded by the Ministry of Education of Korea. This study was supported by 2020 Research Grant from Kangwon National University. The author (D. Jeong) was supported by the National Research Foundation of Korea (NRF) grant funded by the Korea government (MSIP) (NRF-2020R1F1A1A01075937). The corresponding author (J.S. Kim) was supported by Basic Science Research Program through the National Research Foundation of Korea (NRF).

References

[1] J. W. Cahn, "Über die umsetzung an der spinodalen," *Acta Metallurgica*, vol. 9, no. 9, pp. 795–801, 1961.

[2] J. W. Cahn and J. E. Hilliard, "Spinodale entmischung: Eine reprise," *Acta Metallurgica*, vol. 19, no. 2, pp. 151–161, 1971.

[3] J. Erlebacher, M. J. Aziz, A. Karma, N. Dimitrov, and K. Sieradzki, "Evolution of nanoporosity in dealloying," *Nature*, vol. 410, no. 6827, pp. 450–453, 2001.

[4] M. Khenner and V. Henner, "Modeling evolution of composition patterns in a binary surface alloy," *Modelling and Simulation in Materials Science and Engineering*, vol. 29, no. 1, p. 015002, 2021.

[5] I. S. Menshov and C. Zhang, "Interface capturing method based on the Cahn–Hilliard equation for two-phase flows," *Computational Mathematics and Mathematical Physics*, vol. 60, no. 3, pp. 472–483, 2020.

[6] J. Yang and J. Kim, "A novel Cahn-Hilliard-Navier-Stokes model with a nonstandard variable mobility for two-phase incompressible fluid flow," *Computers and Fluids*, vol. 213, p. 104755, 2020.

[7] J. Yang and J. Kim, "An efficient stabilized multiple auxiliary variables method for the Cahn- Hilliard-Darcy two-phase flow system," *Computers and Fluids*, vol. 223, p. 104948, 2021.

[8] S. Zhou and M. Y. Wang, "Multimaterial structural topology optimization with a generalized Cahn-Hilliard model of multiphase transition," *Structural and Multidisciplinary Optimization*, vol. 33, no. 2, pp. 89–111, 2006.

[9] X. Zhang, A. Takezawa, and Z. Kang, "A phase-field based robust topology optimization method for phononic crystals design considering uncertain diffuse regions," *Computational Materials Science*, vol. 160, pp. 159–172, 2019.

[10] A. Bartels, P. Kurzeja, and J. Mosler, "Cahn-Hilliard phase field theory coupled to mechanics: fundamentals, numerical implementation and application to topology optimization," *Computer Methods in Applied Mechanics and Engineering*, vol. 383, p. 113918, 2021.

[11] D. Cohen and J. M. Murray, "A generalized diffusion model for growth and dispersal in a population," *Journal of Mathematical Biology*, vol. 12, no. 2, pp. 237–249, 1981.

[12] A. C. Aristotelous, O. A. Karakashian, and S. M. Wise, "Adaptive, second-order in time, primitive-variable discontinuous Galerkin schemes for a Cahn-Hilliard equation with a mass source," *IMA Journal of Numerical Analysis*, vol. 35, no. 3, pp. 1167–1198, 2015.

[13] W. Feng, Z. Guo, J. S. Lowengrub, and S. M. Wise, "A mass-conservative adaptive FAS multigrid solver for cell-centered finite difference methods on block-structured, locally-cartesian grids," *Journal of Computational Physics*, vol. 352, pp. 463–497, 2018.

[14] A. Agosti, P. F. Antonietti, P. Ciarletta, M. Grasselli, and M. Verani, "A Cahn–Hilliardtype equation with application to tumor growth dynamics," *Mathematical Methods in the Applied Sciences*, vol. 40, no. 18, pp. 7598–7626, 2017.

[15] A. Oron, S. H. Davis, and S. G. Bankoff, "Long-scale evolution of thin liquid films," *Reviews of Modern Physics*, vol. 69, no. 3, pp. 931–980, 1997.

[16] U. Thiele and E. Knobloch, "Thin liquid films on a slightly inclined heated plate," *Physica D*, vol. 190, no. 3-4, pp. 213–248, 2004.

[17] S. Torabi and J. Lowengrub, "Simulating interfacial anisotropy in thin-film growth using an extended Cahn–Hilliard model," *Physical Review E*, vol. 85, no. 4, p. 041603, 2012.

[18] R. Choksi, M. A. Peletier, and J. F. Williams, "On the phase diagram for microphase separation of diblock copolymers: an approach via a nonlocal Cahn-Hilliard functional," *SIAM Journal on Applied Mathematics*, vol. 69, no. 6, pp. 1712–1738, 2009.

[19] D. Jeong and J. Kim, "Microphase separation patterns in diblock copolymers on curved surfaces using a nonlocal Cahn–Hilliard equation," *The European Physical Journal E*, vol. 38, no. 11, pp. 1–7, 2015.

[20] A. Bertozzi, S. Esedoglu, and A. Gillette, "Inpainting of binary images using the Cahn-Hilliard equation," *IEEE Transactions on Image Processing*, vol. 16, no. 1, pp. 285–291, 2007.

[21] A. Bertozzi, S. Esedoglu, and A. Gillette, "Analysis of a two-scale Cahn-Hilliard model for binary image inpainting," *Multiscale Modeling and Simulation*, vol. 6, no. 3, pp. 913–936, 2007.

[22] Y. Li, D. Jeong, J. Shin, and J. Kim, "A conservative numerical method for the Cahn-Hilliard equation with Dirichlet boundary conditions in complex domains," *Computers & Mathematcs with Applications*, vol. 65, no. 1, pp. 102–115, 2013.

[23] Y. Li, H. G. Lee, B. Xia, and J. Kim, "A compact fourth-order finite difference scheme for the three-dimensional Cahn-Hilliard equation," *Computer Physics Communications*, vol. 200, pp. 108–116, 2016.

[24] Y. Li, Y. Choi, and J. Kim, "Computationally efficient adaptive time step method for the Cahn-Hilliard equation," *Computers & Mathematcs with Applications*, vol. 73, no. 8, pp. 1855–1864, 2017.

[25] Y. Di, Y. Fan, R. Li, and L. Zheng, "Linear stability of hyperbolic moment models for Boltzmann equation," *Numerical Mathematics: Theory, Methods and Applications*, vol. 10, no. 2, pp. 255–277, 2017.

[26] A. Barletta and M. Celli, "Unstable wave-packet perturbations in an advective Cahn–Hilliard process," *Physical Review E*, vol. 99, no. 5, p. 052219, 2019.

[27] J. Shen, T. Tang, and L. L. Wang, "Spectral methods: algorithms analysis and applications," *Springer Science & Business Media*, vol. 41, pp. 23–46, 2011.

[28] S. Lee, C. Lee, H. G. Lee, and J. Kim, "Comparison of different numerical schemes for the Cahn–Hilliard equation," *Journal of the Korean Society for Industrial and Applied Mathematics*, vol. 17, no. 3, pp. 197–207, 2013.

[29] A. Shah, M. Sabir, and S. Ayub, "An adaptive time-stepping scheme for the numerical simulation of Cahn-Hilliard equation with variable mobility," *Journal of applied mathematics and mechanics*, vol. 99, no. 7, p. e201800246, 2019.